



The Small Sizes and High Implied Densities of “Little Red Dots” with Balmer Breaks Could Explain Their Broad Emission Lines without an Active Galactic Nucleus

Josephine F. W. Baggen¹ , Pieter van Dokkum¹ , Gabriel Brammer² , Anna de Graaff³ , Marijn Franx⁴ , Jenny Greene⁵ , Ivo Labbé⁶ , Joel Leja^{7,8,9} , Michael V. Maseda¹⁰ , Erica J. Nelson¹¹ , Hans-Walter Rix³ , Bingjie Wang (王冰洁)^{7,8,9} , and Andrea Weibel¹²

¹ Department of Astronomy, Yale University, New Haven, CT 06511, USA; josephine.baggen@yale.edu

² Cosmic Dawn Center (DAWN), Niels Bohr Institute, University of Copenhagen, Jagtvej 128, København N, DK-2200, Denmark

³ Max-Planck-Institut für Astronomie, Königstuhl 17, D-69117, Heidelberg, Germany

⁴ Leiden Observatory, Leiden University, P.O. Box 9513, NL-2300 RA Leiden, The Netherlands

⁵ Department of Astrophysical Sciences, Princeton University, 4 Ivy Lane, Princeton, NJ 08544, USA

⁶ Centre for Astrophysics and Supercomputing, Swinburne University of Technology, Melbourne, VIC 3122, Australia

⁷ Department of Astronomy & Astrophysics, The Pennsylvania State University, University Park, PA 16802, USA

⁸ Institute for Computational & Data Sciences, The Pennsylvania State University, University Park, PA 16802, USA

⁹ Institute for Gravitation and the Cosmos, The Pennsylvania State University, University Park, PA 16802, USA

¹⁰ Department of Astronomy, University of Wisconsin-Madison, 475 N. Charter St., Madison, WI 53706, USA

¹¹ Department for Astrophysical and Planetary Science, University of Colorado, Boulder, CO, USA

¹² Department of Astronomy, University of Geneva, Chemin Pegasi 51, 1290 Versoix, Switzerland

Received 2024 August 15; revised 2024 October 30; accepted 2024 November 08; published 2024 December 6

Abstract

Early JWST studies found an apparent population of massive, compact galaxies at redshifts $z \gtrsim 7$. Recently three of these galaxies were shown to have prominent Balmer breaks, demonstrating that their light at $\lambda_{\text{rest}} \sim 3500 \text{ Å}$ is dominated by a stellar population that is relatively old ($\sim 200 \text{ Myr}$). All three also have broad $H\beta$ emission with $\sigma > 1000 \text{ km s}^{-1}$, a common feature of such “little red dots.” From Sérsic profile fits to the Near Infrared Camera images in F200W we find that the stellar light of galaxies is extremely compact: the galaxies have half-light radii of $r_e \sim 100 \text{ pc}$, in the regime of ultracompact dwarfs in the nearby Universe. Their masses are uncertain, as they depend on the contribution of possible light from an active galactic nucleus (AGN) to the flux at $\lambda_{\text{rest}} > 5000 \text{ Å}$. If the AGN contribution is low beyond the Balmer break region, the masses are $M_* \sim 10^{10} - 10^{11} M_\odot$, and the central densities are higher than those of any other known galaxy population by 1 order of magnitude. Interestingly, the implied velocity dispersions of $\sim 1500 \text{ km s}^{-1}$ are in very good agreement with the measured $H\beta$ line widths. We suggest that some of the broad lines in “little red dots” are not due to AGNs, but simply reflect the kinematics of the galaxies, and speculate that the galaxies are observed in a short-lived phase where the central densities are much higher than at later times. We stress, however, that the canonical interpretation of AGNs causing the broad $H\beta$ lines also remains viable.

Unified Astronomy Thesaurus concepts: Galaxies (573); High-redshift galaxies (734); Compact galaxies (285); Galaxy spectroscopy (2171); Active galaxies (17); Galactic and extragalactic astronomy (563)

1. Introduction

The James Webb Space Telescope (JWST) has revealed a population of high-redshift objects with very specific spectral energy distributions (SEDs): a flat blue continuum and a steep red slope (e.g., D. D. Kocevski et al. 2023; I. Labbé et al. 2023b, 2023a; Y. Ono et al. 2023; M. Onoue et al. 2023; H. B. Akins et al. 2024; G. Barro et al. 2024). They are often compact (H. B. Akins et al. 2023; J. F. W. Baggen et al. 2023), appearing as “little red dots” (LRDs; J. Matthee et al. 2024), and some, but not all, are confirmed to have moderately broad ($\text{FWHM} \sim 1200 - 4000 \text{ km s}^{-1}$) Balmer lines in their spectra (e.g., Y. Harikane et al. 2023b; M. Killi et al. 2024; D. D. Kocevski et al. 2023, 2024; V. Kokorev et al. 2023, 2024; R. L. Larson et al. 2023; R. Maiolino et al. 2024b; H. Übler et al. 2023; J. E. Greene et al. 2024; J. Matthee et al. 2024; B. Wang et al. 2024a, 2024b). The most straightforward interpretation of the small sizes and broad

Balmer lines is that we are seeing active galactic nuclei (AGNs) with a broad-line region (BLR). If they are AGNs, they are unusual: they are typically not detected in X-ray emission (H. B. Akins et al. 2024; T. T. Ananna et al. 2024; L. J. Furtak et al. 2024; J. E. Greene et al. 2024; M. Kokubo & Y. Harikane 2024; R. Maiolino et al. 2024a; M. Yue et al. 2024); have yet to demonstrate photometric variability in the Near Infrared Camera (NIRCam; M. Kokubo & Y. Harikane 2024); have flat SEDs in the mid-far-IR for some LRDs, implying dominant contribution from stars at these wavelengths (P. G. Pérez-González et al. 2024); show no dominant contribution from hot dust emission expected from an AGN at rest-frame $3 \mu\text{m}$ (C. C. Williams et al. 2024); and have not been detected in stacks of mid-IR/far-IR/submillimeter/radio data (H. B. Akins et al. 2024).

The correct interpretation of these galaxies—whether they are dominated by AGNs or are compact and massive—has far-reaching implications for black hole physics (e.g., Á. Bogdan et al. 2024; J. E. Greene et al. 2024; K. Inayoshi & K. Ichikawa 2024; I. Juodžbalis et al. 2024b; O. E. Kovács et al. 2024; R. Maiolino et al. 2024a), the theory of galaxy formation and



Original content from this work may be used under the terms of the [Creative Commons Attribution 4.0 licence](https://creativecommons.org/licenses/by/4.0/). Any further distribution of this work must maintain attribution to the author(s) and the title of the work, journal citation and DOI.

evolution (e.g., A. Loeb 2024; J. Silk et al. 2024), and perhaps even cosmology (M. Boylan-Kolchin 2023).

Recently, three LRDs at redshifts $z = 6.8\text{--}8.4$ were shown to have prominent Balmer breaks in their JWST spectra (B. Wang et al. 2024b). Two of these galaxies are among the massive galaxy candidates reported in I. Labbé et al. (2023b). The Balmer break indicates the presence of an evolved stellar population, with stellar ages of more than 100 Myr (A. G. Bruzual 1983; D. Hamilton 1985; G. Worthey et al. 1994; M. L. Balogh et al. 1999; B. M. Poggianti et al. 1999), and their detection strongly suggests that the SEDs at $\lambda_{\text{rest}} \sim 3500 \text{ \AA}$ are not dominated by AGNs. However, all three objects also have broad $H\beta$ emission lines ($\sigma_{H\beta} > 1000 \text{ km s}^{-1}$), suggesting that AGNs are present. B. Wang et al. (2024b) fit the SEDs of the three galaxies and show that the derived stellar population parameters depend sensitively on the interpretation of the continuum redward of the Balmer break. Equally good fits are obtained using either a model with a high stellar mass and extended star formation history, a model with a dust-obscured AGN with minimal stellar mass, or a solution in between. This leads to a wide range of stellar masses ($M_* \sim 10^9\text{--}10^{11} M_\odot$), and the implied possible natures and evolutionary tracks of these sources range from the progenitors of massive ellipticals to low-mass galaxies with overmassive black holes.

In this Letter, we use the fact that we know both the redshifts of these galaxies and that the extended light in the UV suggests that the light at these wavelengths is dominated by stars to measure accurate half-light radii. This follows our initial size measurements (J. F. W. Baggen et al. 2023) of the I. Labbé et al. (2023b) galaxies that were based on photometric redshifts and earlier versions of the imaging data. We then use the previously determined masses for different AGN contributions, combined with the sizes, to measure densities and predict emission line widths and compare these to the observed line widths. Throughout this work we assume Λ CDM cosmology with $H_0 = 70 \text{ km s}^{-1} \text{ Mpc}^{-1}$, $\Omega_{m,0} = 0.3$, and $\Omega_{\Lambda,0} = 0.7$. Magnitudes are reported in the AB system.

2. Data

2.1. Imaging

The JWST NIRCам imaging data of this Letter are obtained from the Cosmic Evolution Early Release Science (CEERS) program (PI: Finkelstein, PID: 1345; S. L. Finkelstein et al. 2022, 2023a; see data DOI of S. L. Finkelstein et al. 2023b). In this work, we use the mosaics available through the DAWN JWST Archive (DJA, v7.2), which are reduced using the GRIZLI pipeline (G. Brammer 2023). The mosaics are available in six broadband filters, short wavelength (SW; F115W, F150W, and F200W) and long wavelength (LW; F277W, F356W, and F444W) with a resolution of $0''.04 \text{ pix}^{-1}$. In addition, higher-resolution ($0''.02 \text{ pix}^{-1}$) data are available for the SW bands, for which the mosaics are split into 12 tiles (ceers-full-xi.yj-v7.2-f200w-clear_drc_sci.fits.gz, where i runs from 0 to 5 and j from 0 to 1.). Ideally, we would use the band at the location of the Balmer break ($\sim 3 \mu\text{m}$) to do the analysis. However, due to the large pixel size (and the broader point-spread function (PSF)) of the LW data, the galaxies are barely resolved/unresolved at these wavelengths. Therefore, we use F200W for our analysis, the reddest band available with 20 mas sampling. Moreover, the F200W filter probes the highest

signal-to-noise ratio out of all the SW filters. We show cutouts and red, green, and blue (RGB) images (see Figure 1) of the galaxies using multiple bands for illustration.

Compared to previous versions (e.g., v4 used in I. Labbé et al. 2023b; J. F. W. Baggen et al. 2023), the weighting scheme to do the drizzling has changed. Previously, the weighting was done including the Poisson noise from the source. This caused a suppression of flux in the central pixels for compact sources, which could directly affect the sizes of sources in the images. As we show in this work, the two sources (L23-38094 and L23-14924) for which the sizes are also reported in J. F. W. Baggen et al. (2023), the newly measured sizes are indeed smaller in the new reductions.

The form of the PSF, which describes how point sources appear in the data, is a crucial aspect of the analysis, yet complicated to model properly. One approach is to create an empirical PSF from either bright, well-centered single stars or by stacking multiple stars in the mosaic. Another approach is forward modeling of the telescope instruments, as is done for the WebbPSF tool created for JWST imaging (J. M. Oschmann et al. 2014). The advantage of these synthetic PSFs is the high signal-to-noise ratios and perfect sampling. However, a variety of studies have found discrepancies between WebbPSF profiles and point sources in the images (X. Ding et al. 2022; Y. Ono et al. 2023; M. Onoue et al. 2023; J. R. Weaver et al. 2024).

We first consider a PSF made from stacking of centered, bright, unsaturated stars in the entire mosaic (as described in A. Weibel et al. 2024). However, we find that this PSF gives large ellipticities (and a very similar position angle) when fit to compact galaxies. Furthermore, the light profile is clearly broader than that of single, well-centered stars in the vicinity of the three galaxies. Therefore, we also consider five single stars (R.A. [214.958582, 214.950395, 214.97986, 214.827323, 214.802483], decl. [52.930525, 52.946655, 52.969334, 52.8194630, 52.837142]), that are bright and close to the galaxies. This method avoids smoothing due to stacking and implicitly accounts for local variations of the PSF. Although all of these stars give very similar results, none of the stars are perfectly centered (>0.1 pixel shift in x and y).

Finally, we inspect results from synthetic WebbPSF models. These fits are almost identical to those from single stars. Given the reproducibility of WebbPSF, we use this for our reported measurements. The uncertainty in the PSF is taken into account in the error analysis, where we use both WebbPSF, single stars, and the stacked empirical PSF (see Section 3.3).

2.2. Spectra

The spectroscopic properties of the three LRDs¹³ with Balmer breaks shown in this Letter are obtained from B. Wang et al. (2024b). Briefly, the galaxies were selected from a spectroscopic follow-up program RUBIES (JWST-GO-4233, PIs: A. de Graaff & G. Brammer; A. de Graaff et al. 2024) that uses the NIRSpec microshutter array (MSA). The RUBIES selection partially overlaps with the double break candidates of I. Labbé et al. (2023b). The sources were targeted and observed in 2024 March for 48 minutes in the Prism/Clear mode and the

¹³ These sources have $m_{F277W} - m_{F444W} > 1.5$, $m_{F444W} < 26$, similar to definitions of LRDs of G. Barro et al. (2024), H. B. Akins et al. (2024), and P. G. Pérez-González et al. (2024). These sources also have broad Balmer emission lines, following the original criteria of J. Matthee et al. (2024), even though that was not a selection criterion a priori.

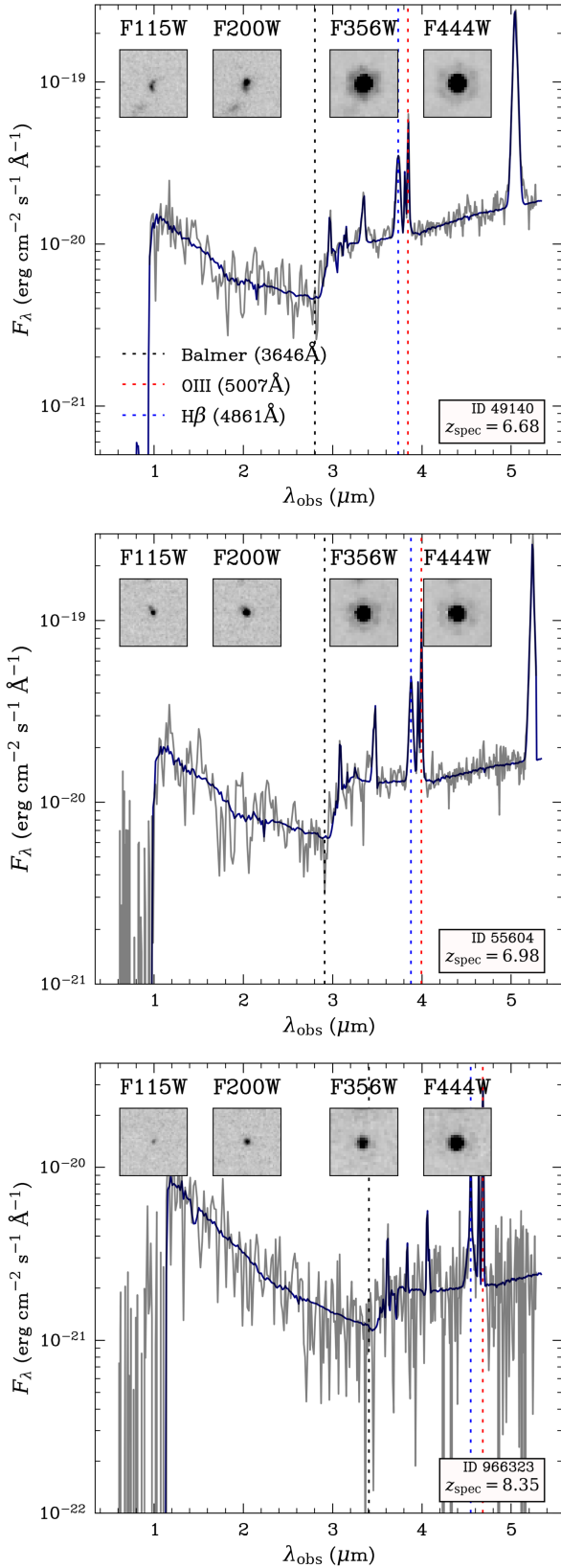


Figure 1. The spectra (gray) and best-fit model (dark blue) with maximal stellar mass of three Balmer break galaxies, obtained from B. Wang et al. (2024b). We also show $1'' \times 1''$ images in four different bands, F115W, F200W, F356W, and F444W. The dotted lines indicate the location of the Balmer break (black), [O III] line (red), and H β (blue) line, which are relevant in this work. For information on other emission lines, see B. Wang et al. (2024b).

G395M/F290LP mode. For more information on the reduction, we refer to K. E. Heintz et al. (2024).

The modeling of the spectra is described in B. Wang et al. (2024b). Briefly, three different limiting cases are adopted to decompose the continuum into a stellar and AGN component. The first model maximizes the stellar contribution and minimizes the AGN contribution to the continuum, by setting it to zero. The resulting stellar masses of all three galaxies are very high, $M_{*,\text{max}} \sim 10^{11} M_{\odot}$. In the cumulative stellar mass density versus stellar mass plane, they lie close to the limit allowed by Λ CDM (see both M. Boylan-Kolchin 2023; B. Wang et al. 2024b). The second model assumes a maximal AGN contribution and therefore minimizes the contribution of stars. These minimal masses are $M_{*,\text{min}} \sim 10^9 M_{\odot}$. As described in B. Wang et al. (2024b), this model leads to overmassive black holes relative to their host stellar masses, compared to the local relation. They also adopt a third model that lies in between the “maximum” and “minimum” cases, with stellar masses of $M_{*,\text{med}} \sim 10^{10} M_{\odot}$. In this model, the AGN and stellar population both contribute equally to the red continuum at $\lambda_{\text{rest}} \sim 5000 \text{ \AA}$, while the AGN dominates the red continuum beyond that wavelength.

While these three models are physically very different, they give equally good fits to the red continuum. This is problematic for determining the stellar masses, which are not well constrained, with differences in stellar mass between the no-AGN and max AGN models of up to ~ 2 dex. Other caveats complicate the determination of stellar masses even further, such as the assumption of an initial mass function (IMF; see, e.g., P. van Dokkum & C. Conroy 2024) and the lack of information at near-infrared wavelengths from for example MIRI (H. B. Akims et al. 2024; T. Wang et al. 2024c). These uncertainties are smaller than those associated with the choice of AGN contribution (see, e.g., C. Conroy et al. 2009), but we stress that there are significant systematic uncertainties even within each of the three B. Wang et al. (2024b) models. In this work, we adopt the reported stellar masses from B. Wang et al. (2024b), derived from the spectra in rest-frame UV to optical and a G. Chabrier (2003) IMF, but we stress the caveats involved in these stellar mass measurements. Finally, we consider the three cases that vary the contribution of AGN as possible truths. The nine individual stellar mass measurements are listed in Table 1. For more information on the fitting procedure and parameters in the modeling of the three scenarios, we refer to B. Wang et al. (2024b).

In Figure 1 we show the spectra in light gray and the best-fit model using the maximum stellar mass in dark blue. For illustration we also show the Balmer break at $\lambda_{\text{rest}} = 3646 \text{ \AA}$, the [O III] line at $\lambda_{\text{rest}} = 5007 \text{ \AA}$, and H β at $\lambda_{\text{rest}} = 4861 \text{ \AA}$ as dotted lines in black, red, and blue, respectively.

3. Structural Properties

3.1. Morphologies

In Figure 2 (top panels) we show the individual images ($1'' \times 1''$) for the three Balmer break galaxies in F200W, as well as the NIRSpec slits that were used. We also show two RGB images, the first created from cutouts in F115W (blue), F150W (green), and F200W (red) and the second from F150W (blue), F277W (green), and F444W (red). The images show that all three galaxies are extremely small and appear as single,

Table 1
Spectroscopic and Structural Properties of Three Balmer Break Galaxies

RUBIES-ID	L23-ID	R.A.	Decl.	z_{spec}	$\log(M_{*,\text{max}})$ (M_{\odot})	$\log(M_{*,\text{med}})$ (M_{\odot})	$\log(M_{*,\text{min}})$ (M_{\odot})	$\sigma(\text{H}\beta)$ (km s^{-1})	$r_{\text{e, maj}}$ (pc)	b/a
49140		214.89225	52.87741	6.68	$11.2^{+0.15}_{-0.14}$	$9.93^{+0.22}_{-0.14}$	$9.50^{+0.08}_{-0.09}$	1402^{+68}_{-79}	123^{+173}_{-45}	0.58
55604	38904	214.98303	52.95600	6.98	$11.1^{+0.15}_{-0.16}$	$9.79^{+0.14}_{-0.14}$	$8.99^{+0.16}_{-0.14}$	1527^{+106}_{-115}	54^{+53}_{-43}	0.78
966323	14924	214.87615	52.88083	8.35	$10.6^{+0.13}_{-0.49}$	$9.84^{+0.20}_{-0.32}$	$8.72^{+0.21}_{-0.19}$	1369^{+280}_{-315}	86^{+9}_{-42}	0.73

Note. The first and second columns indicate the galaxy ID given in B. Wang et al. (2024b) and the corresponding ID number of L23. The spectroscopic redshift (column (4)), stellar masses (M_{\odot}) with 1σ errors (columns (4)–(6)) and velocity dispersion (km s^{-1}) of the broad H β line (column (7)) are obtained from B. Wang et al. (2024b). The three different stellar masses are obtained by varying the AGN contribution relative to stellar contribution (see the text). Columns (8) and (9) are the fitted effective radii $r_{\text{e, maj}}$ (pc) along the major axis and the minor-to-major axis ratio (b/a), respectively. The galaxies are fit with a Sérsic profile in filter F200W using WebbPSF. We perform simulations (see the text) to obtain 1σ errors on the size measurements.

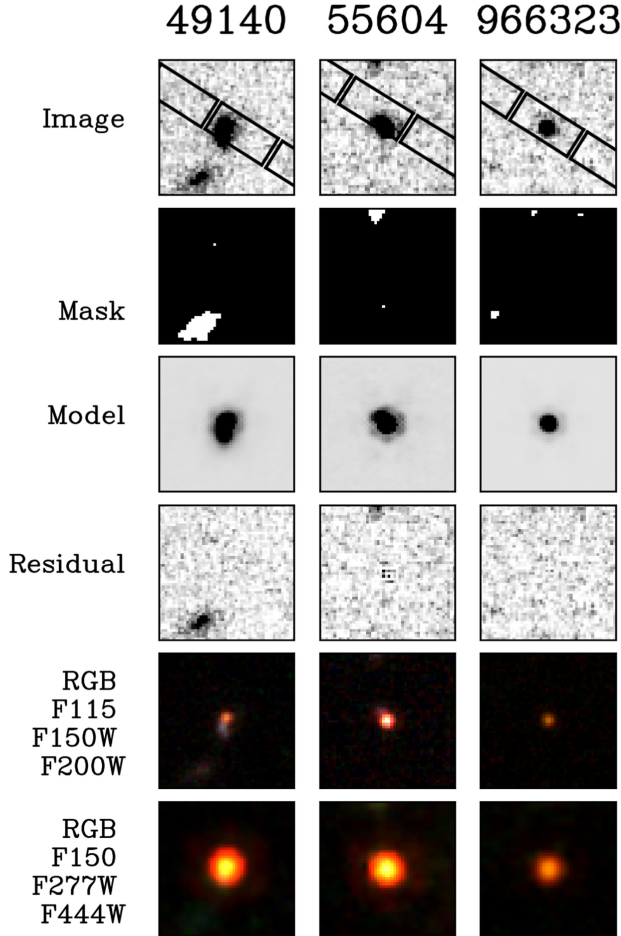


Figure 2. The top row shows images in the NIRC2 F200W band of the three Balmer break galaxies. The second row shows the segmentation maps; the third row shows the best-fitting PSF-convolved GALFIT models. The residuals, obtained by subtracting the best-fitting models from the images, are shown in the fourth row. The fifth row shows RGB images of the galaxies, with F115W as the blue band, F150W as the green band, and F200W as the red band and the final row with F115W, F277W, and F444W. All images are $1'' \times 1''$.

unresolved or barely resolved objects in the long-wavelength bands. However, the morphologies of two of the galaxies are more complex in the bluer bands. ID-49140 and ID-55604 have a faint extension or small clump next to a compact primary component. These clumps are most prominent in F115W (see the cutout images in Figure 1). The morphology of ID-966323 is more pointlike in all bands.

3.2. Sérsic Profile Fitting

We fit the surface brightness profiles of the three Balmer break galaxies with J. L. Sérsic (1968) profiles. As explained in Section 2.1 the fits are done in F200W, probing rest-frame wavelengths of $\lambda_{\text{rest}} \sim 200\text{--}250$ nm. We use GALFIT (C. Y. Peng et al. 2002, 2010), and the relevant parameters are the central position (x, y), the effective radius (along the major axis) (r_{e}), the Sérsic index (n), the total integrated magnitude, the projected minor-to-major axis ratio (b/a), and the position angle (PA).

Initial fits showed that the Sérsic index cannot be determined robustly, given the small sizes of the galaxies, but that it typically ranges between 1 and 3.5. We adopt a fixed $n = 1.5$ in the fits. The uncertainty in n translates into an uncertainty in r_{e} , and this is propagated in our error analysis (see Section 3.3). The r_{e} is allowed to vary between 0.01 and 100 pixels and the total integrated magnitude between -5 and $+5$ mag from the previously measured aperture magnitude.

We generate a mask with contaminating sources as follows. The background is estimated using sigma-clipped statistics with a filter size of 5 pixels and the background rms (σ). After subtracting the background, the data are convolved with a 2D Gaussian kernel with an FWHM of 3 pixels. Using this convolved background-subtracted image, we adopt a source detection threshold of 1.5σ . The resulting map contains pixels that are not considered while fitting the galaxy models on the image with GALFIT.

For ID-55604 and ID-49140, we fit two Sérsic components based on the images in F115W and F150W (see Section 3.1). The nature of the relatively blue secondary, offset, components is unclear. The primary component contains 70% and 85% of the total fluxes of ID-55604 and ID-49140, respectively. As the primary components are redder than the secondary components (particularly for ID-55604—see Figure 2), they contribute an even larger fraction of the total masses. Fitting the galaxies with single components leads to significant residuals, as expected, and sizes that are twice as large as our default values. We include this systematic uncertainty in the error bars of these objects, as discussed in Section 3.3.

3.3. Sizes and Uncertainties

The masks, best-fitting models, and residuals from the fits are shown in Figure 2. The fits are overall excellent. The effective radii are extremely small, ~ 1.1 pixel or smaller. Using the spectroscopic redshifts of the galaxies, we find physical effective radii of 123, 54, and 86 pc for the three galaxies. To determine the uncertainties in these measurements we perform

simulations to obtain upper and lower bounds for the sizes, taking into account the assumptions and unknowns in the modeling.

For each galaxy we consider a finely sampled array of possible sizes, from 0 to several pixels. For each test size $r_{e,\text{test}}$ we simulate 10^3 Sérsic models using GALFIT, with $r_e = r_{e,\text{test}}$ and the same integrated magnitude of the best-fit model, while randomly assigning b/a from 0.1 to 1, PA from 0° to 90° , and n from 0.5 to 6. We convolve these Sérsic models with either the stacked empirical PSF or WebbPSF. We then place these convolved models into the residual maps of the initial fits, so that differences between the galaxy profiles and Sérsic profiles are included in the errors. We fit these synthetic images following the same methodology as was used to fit the galaxies. This includes keeping $n = 1.5$ fixed, fitting with WebbPSF, and solving for r_e , b/a , the integrated magnitude, PA, and the sky background. This results in an array of 10^3 different sizes for which the underlying model had a true size of $r_{e,\text{test}}$. Next, we ask whether the observed size $r_{e,\text{obs}}$ is within the central 68% of the distribution of 10^3 simulated sizes. If so, then $r_{e,\text{test}}$ is deemed an acceptable true size of the object, and it is included in the 1σ error bar for that galaxy.

We find that the uncertainties are asymmetric, with smaller true sizes being more likely than larger true sizes. This can be traced to two effects. First, our choice of the WebbPSF for the default measurement: convolving a galaxy with an empirical PSF and then fitting it with WebbPSF leads to a slight (~ 0.2 pixel) overestimate of the size, and as half the simulations use empirical PSFs this leads to an overall bias in the simulated sizes. Second, there are more simulations with $n > 1.5$ than with $n < 1.5$, and fitting with fixed $n = 1.5$ leads to a small (also ~ 0.2 pixels) bias.

A final uncertainty that has to be taken into account is our choice of fitting two galaxies (ID-55604 and ID-49140) with two components rather than one. We refit both galaxies with a single component to assess the importance of this choice. These fits lead to strong residuals, but they are stable. The half-light radii of both galaxies increase by a factor of ~ 2 when they are fit as a single component. To account for this, we add the difference between the single-component and two-component fits in quadrature to the (positive) error bars of these two galaxies. In Table 1 we report the measured sizes with their uncertainties.

3.4. Size–Luminosity Relation

The central observational result of this Letter is the compactness of the three Balmer break galaxies at $z \sim 7$ –8. The sizes for ID-55604 and ID-966323 are lower than measured in J. F. W. Baggen et al. (2023) for identical galaxies due to the new reduction scheme (see Section 2), but are consistent within the error bars. The average size of the three galaxies is $\langle r_e \rangle \approx 90$ pc, smaller than the mean size of 150 pc in J. F. W. Baggen et al. (2023).

The sizes are similar to those of ultracompact dwarf galaxies ($r_{\text{eff}} \leq 100$ pc; e.g., H.-X. Zhang et al. 2015) and smaller than any other moderately luminous galaxy population observed at $0 < z < 5$. To illustrate the extreme nature of these objects, we show the relation between effective radius (along the major axis) and UV magnitude ($\lambda_{\text{rest}} \sim 1500$ Å) in Figure 3. Besides the three Balmer break galaxies we show the relation for local spiral galaxies, obtained from R. S. de Jong & C. Lacey (2000), for which we correct the measured i -band magnitudes to UV

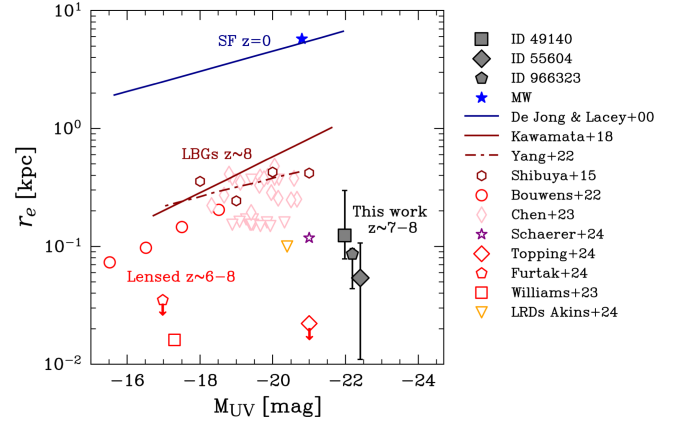


Figure 3. The size measured in F200W, plotted against the UV magnitude, measured from the spectrum at $\lambda_{\text{rest}} = 150$ nm. We also show size–luminosity derived for local spiral galaxies from R. S. de Jong & C. Lacey (2000) for which we use a magnitude correction $M_{\text{UV}} - M_i = 1.0$, and LBGs at $z \sim 8$ (T. Shibuya et al. 2015; R. Kawamata et al. 2018; R. J. Bouwens et al. 2022) and $z \sim 9$ –12 (L. Yang et al. 2022). In addition we show star-forming complexes (Z. Chen et al. 2023) with $z_{\text{phot}} \sim 6$ –8. Finally, we show extremely compact sources, recently detected through lensing with JWST, reported in L. J. Furtak et al. (2024; $R_e < 35$ pc, $z = 7.0$), M. W. Topping et al. (2024; $R_e < 22$ pc, $z = 6.1$), and H. Williams et al. (2023; $R_e = 16$ pc, $z = 9.5$). Finally we show the upper limit of $\lesssim 100$ pc reported for the brightest LRDs (H. B. Akins et al. 2024; see the text).

magnitude using $M_{\text{UV}} - M_i = 1.0$, following A. Grazian et al. (2012). We also show the size–luminosity relation for Lyman break galaxies (LBGs) detected prior to JWST at $z \sim 8$ from T. Shibuya et al. (2015), R. Kawamata et al. (2018), and R. J. Bouwens et al. (2022), as well as recently detected galaxies with JWST at $z \sim 9$ –12 from L. Yang et al. (2022). At fixed absolute magnitude, these galaxies are about $100\times$ smaller than local spiral galaxies and about $10\times$ smaller than LBGs at the same redshifts. Instead, their sizes are similar to those of lensed sources, reported in R. J. Bouwens et al. (2022), which are ~ 6 mag fainter. However, these sizes corroborate with some of the most recent results with JWST. We show the sizes (diamond) and upper limits (triangle) of star-forming complexes reported in Z. Chen et al. (2023) with $z_{\text{phot}} \sim 6$ –8. In addition, we show a bright compact galaxy at $z_{\text{spec}} = 9.4$ with $R_e = 118$ pc (D. Schaerer et al. 2024b). Extremely compact sources, recently detected through lensing with JWST, reported in L. J. Furtak et al. (2024; $R_e < 35$ pc, $z = 7.0$), M. W. Topping et al. (2024; $R_e < 22$ pc, $z = 6.1$), and H. Williams et al. (2023; $R_e = 16$ pc, $z = 9.5$) are shown as red scatter points. Finally, we show $r_e \leq 100$ as a reference upper limit for the brightest LRDs found by H. B. Akins et al. (2024), and we convert the reported flux at $\lambda_{\text{obs}} = 1.15$ μm ($F = 15.76$ nJy) from the observed stacked spectrum to rest-frame UV magnitude, assuming a redshift of $z = 6$.

4. Densities and Kinematics

The small sizes, combined with the masses determined in B. Wang et al. (2024b), imply very high densities. Here we assess the average surface density of the galaxies (Section 4.1), their 3D density profiles (Section 4.2), and the expected kinematics (Section 4.3). In each subsection we consider all three mass measurements of B. Wang et al. (2024b), for minimal, medium, and maximal AGN contributions, and indicate those with different colors in the figures.

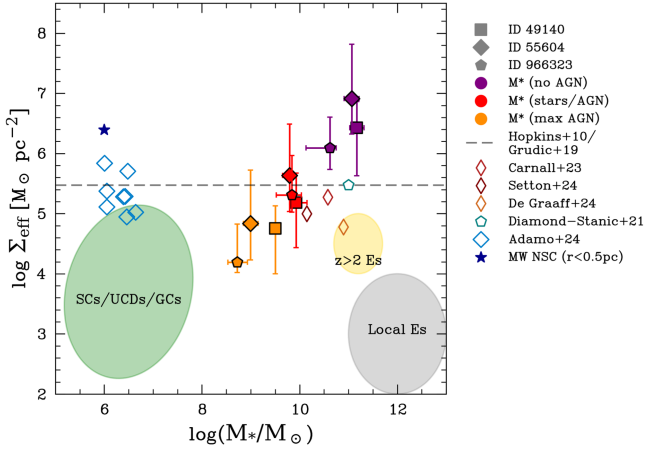


Figure 4. The surface density ($\Sigma_{\text{eff}} = M_*(\leq R_e)/\pi R_e^2$) plotted against stellar mass. We show a theoretical limit $\Sigma_{\text{eff}} \leq 3 \times 10^5 M_\odot \text{pc}^{-2}$, determined by M. Y. Grudić et al. (2019), as the dashed black line. For illustration, we show regions in M_* – Σ_{eff} space for multiple stellar systems estimated from P. F. Hopkins et al. (2010), the class of star clusters (SCs), ultracompact dwarf galaxies (UCDs), and globular clusters (GCs) (green); local elliptical galaxies (gray); and compact $z > 2$ elliptical galaxies (yellow). We also show (see the text) quiescent galaxies at $z \sim 4$ –5 (A. C. Carnall et al. 2023; A. de Graaff et al. 2024; D. J. Setton et al. 2024), compact starburst galaxies at $z = 0.4$ –0.8 (A. M. Diamond-Stanic et al. 2021), Cosmic Gems star clusters at $z \sim 10$ (A. Adamo et al. 2024), and the MW nuclear star cluster. The surface density measured for the three Balmer break galaxies are shown for the three sets of stellar masses $M_{*,\text{min}}$, $M_{*,\text{med}}$, and $M_{*,\text{max}}$ in orange, red, and purple, respectively.

4.1. Effective Surface Density

The average surface density within the effective radius can be calculated with

$$\Sigma_{\text{eff}} = M_*(\leq R_e)/\pi R_e^2, \quad (1)$$

where $M_*(\leq R_e) = M_*/2$ and R_e is the projected circularized half-stellar mass–radius $R_e = r_{e, \text{maj}} \sqrt{b/a}$ (ignoring M/L gradients).

In Figure 4 we show the surface densities for the three galaxies and for the three different stellar mass measurements of B. Wang et al. (2024b), $M_{*,\text{min}}$, $M_{*,\text{med}}$, and $M_{*,\text{max}}$ in orange, red, and purple, respectively. For context, we also show regions in M_* – Σ_{eff} space for various stellar systems, as estimated in P. F. Hopkins et al. (2010). Nuclear star clusters, ultracompact dwarf galaxies, dSph nuclei, and globular clusters are taken together and shown in green; local elliptical galaxies are shown in gray; and compact $z > 2$ elliptical galaxies are shown in yellow. We also show recently discovered star clusters at $z \sim 10$ (A. Adamo et al. 2024) in the Cosmic Gems arc.

In addition, we show the surface densities derived for three quiescent massive galaxies at $z = 4$ –5 from A. C. Carnall et al. (2023), A. de Graaff et al. (2024), and D. J. Setton et al. (2024). For these quiescent galaxies the effective radii are circularized using $b/a = 0.7$, identical to the value reported for the compact component in D. J. Setton et al. (2024). Finally, we show the central surface densities for the compact starburst galaxies at $z = 0.4$ –0.8 (A. M. Diamond-Stanic et al. 2021).

The black dashed line shows an effective surface stellar mass density of $\Sigma_{\text{eff}} \leq 3 \times 10^5 M_\odot \text{pc}^{-2}$. In the local Universe, very few stellar systems exceed this limit, going all the way from star clusters and globular clusters to elliptical galaxies (P. F. Hopkins et al. 2010; M. Y. Grudić et al. 2019). It has been suggested that some universal mechanism controls the

surface density: P. F. Hopkins et al. (2010) propose that feedback from massive stars in the form of winds and radiation fields is likely responsible for the observed Σ_{max} . M. Y. Grudić et al. (2019) propose an alternative model, relating the stellar feedback and star formation efficiency (SFE).

The surface densities of the three galaxies discussed here are extremely high. They are above the empirical surface density limit of P. F. Hopkins et al. (2010) by 1 order of magnitude in the no-AGN model, are on the limit for the mixed model, and are below the limit only for the maximal AGN model. The densities are also higher by several orders of magnitude than those of plausible descendants, elliptical galaxies at $z = 0$.

The densities are most extreme for the no-AGN model, and this could be taken as evidence against it. However, we note that some nuclear star clusters reach $\sim 10^6 M_\odot \text{pc}^{-2}$ in their centers, above the empirical limit. An important example is the nuclear star cluster in the center of the Milky Way around SgrA*, which reaches $2.5 \times 10^6 M_\odot \text{pc}^{-2}$ within the central 0.5 pc (see the review by N. Neumayer 2017), indicated in Figure 4 as a dark blue star. We calculated this surface density using a stellar mass within this region of $M_* \sim 10^6 M_\odot$ (R. Schödel et al. 2009).

4.2. Stellar Mass Profiles

As first discussed in R. Bezanson et al. (2009), extreme densities within the effective radius do not necessarily correspond to extreme densities on small physical scales. The effective radius evolves, and if galaxies grow inside out, their surface density within the effective radius goes down with time even if their density within a fixed small physical radius remains constant.

Following J. F. W. Baggen et al. (2023) we show the 3D density profiles of the galaxies in Figure 5. The profiles were determined from the radii and the three different sets of stellar masses, using the same methodology as in J. F. W. Baggen et al. (2023). In short, we perform an Abel transform to the 2D best-fit Sérsic profile (see Table 1). After that, the luminosity profile is converted into a stellar mass profile by assuming the M/L ratio does not change with radius. The profile is then scaled such that the total stellar masses are identical to those derived in B. Wang et al. (2024b). The uncertainty bands reflect the uncertainties in both the radii and the masses. We also show the stellar mass profiles of massive quiescent galaxies at different cosmic times: $z \sim 0$ elliptical galaxies (T. Tal et al. 2009), $z \sim 2.3$ compact elliptical galaxies from R. Bezanson et al. (2009), and the mean mass profile for three quiescent galaxies at $z \sim 4$ –5 (A. C. Carnall et al. 2023; A. de Graaff et al. 2024; D. J. Setton et al. 2024).

We find that the central stellar mass densities are similar to those of plausible descendants for the medium mass model (red points) and that they are lower for the lowest masses (the maximal AGN model). Strikingly, the central densities are extremely high for the no-AGN masses (purple): $\sim 10^{13} M_\odot \text{kpc}^{-3}$ in the inner tens of parsecs, comparable to the densest nuclear star clusters (R. Pechetti et al. 2020). They are 1 order of magnitude above the density of plausible $z \sim 0$ descendants, and also higher (by a factor of ~ 5) than quiescent galaxies at $z = 4$ –5. If the no-AGN stellar masses are correct, it means that inside-out growth alone is not sufficient to connect these galaxies to their plausible descendants. The densities need to evolve downward in order to be consistent with the central

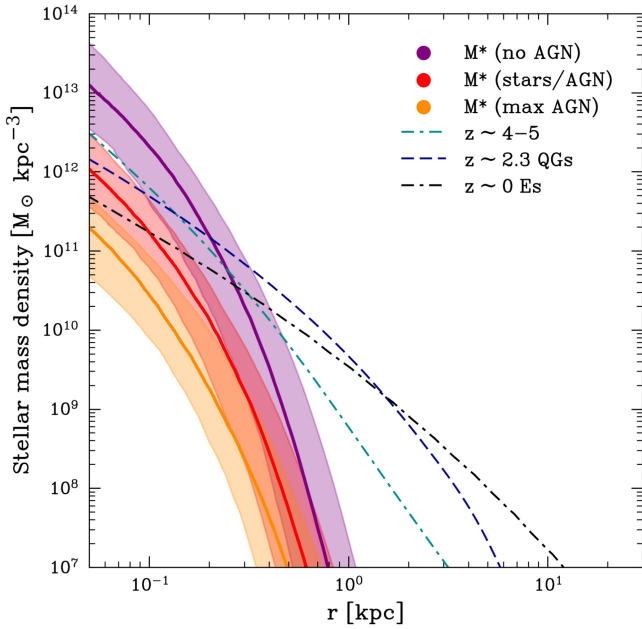


Figure 5. The median stellar mass profiles for the three sets of stellar masses (see Table 1), $M_{*,\min}$, $M_{*,\text{med}}$, and $M_{*,\max}$ in orange, red, and purple, respectively. We also show the stellar mass profiles of massive quiescent galaxies at different cosmic times: the mean stellar mass profile of three compact massive quiescent galaxies at $z \sim 4-5$ (A. C. Carnall et al. 2023; D. J. Setton et al. 2024; A. de Graaff et al. 2024), $z \sim 2.3$ compact elliptical galaxies (R. Bezanson et al. 2009), and massive elliptical galaxies at $z = 0$ (T. Tal et al. 2009).

densities in the cores of quiescent galaxies at $z = 0-5$. We return to this in Section 5.

4.3. Kinematics

From a simple virial equilibrium argument, we can relate the dynamical mass (M_{dyn}) of a galaxy to its velocity dispersion σ at radius r :

$$\sigma^2 \approx \frac{GM_{\text{dyn}}(<r)}{kr}, \quad (2)$$

for which the virial coefficient k depends on the galaxy structure and the shape of the velocity dispersion profile and is typically assumed to be between ~ 3 and 5 (e.g., M. Cappellari et al. 2006; A. van der Wel et al. 2006; M. Franx et al. 2008; E. N. Taylor et al. 2010). If we make assumptions about the properties of the stars and gas in the system, following, e.g., P. G. van Dokkum et al. (2015), we can also relate the velocity dispersion of the gas to the stellar mass and circularized effective radius:

$$\log(\sigma_{\text{pred}}) = 0.5[\log(M_*) - \log(r_e) - C], \quad (3)$$

where σ_{pred} is in km s^{-1} , M_* is in M_\odot , and r_e is in kpc. The constant C is uncertain, as it depends on the inclination and dynamics of the gas and stars, on their mass contributions, and on their relative spatial distributions. Following P. G. van Dokkum et al. (2015) we adopt $C = 5.9$, but to account for the uncertainties in the properties of the systems, we also consider the relations for $C = 6.1$ (as used in R. Bezanson et al. 2009), which corresponds to $1.25\times$ lower expected velocity dispersions for a given mass and size, and $C = 5.7$ ($1.25\times$ higher dispersions). For convenience,

the full derivation along with all detailed assumptions is provided in the Appendix.

In Figure 6 we compare the expected velocity dispersion calculated with Equation (3) to the measured widths of the $\text{H}\beta$ lines in the three galaxies. The error bars reflect the uncertainties in size and mass. The black error bar in the lower left corner indicates how each measurement would shift horizontally when using $C = 5.7$ (to the right) and $C = 6.1$ (to the left). The expected dispersions are a strong function of the choice of stellar mass, ranging from $\sim 150 \text{ km s}^{-1}$ for the minimal masses to $\gtrsim 1000 \text{ km s}^{-1}$ for the maximal (no-AGN) mass.

Remarkably, the expected dispersions are very similar to the observed $\text{H}\beta$ line widths for the no-AGN model. The implication is that the broad Balmer emission lines in these galaxies could simply be the result of the small sizes and high masses of the galaxies, rather than caused by the BLRs around supermassive black holes (SMBHs). For reference, we also show the strongly lensed red, compact source reported in L. J. Furtak et al. (2023, 2024), which has a superficially similar spectrum to the three Balmer break objects in the present study. The upper limit to the effective radius is $R_e \leq 35 \text{ pc}$, and the stellar mass for an SED dominated by stars is $\log(M_*/M_\odot) = 10.57^{14}$ for this object. This gives an expected velocity dispersion (lower limit) similar to the reported value from the $\text{H}\beta$ line ($\sigma = \text{FWHM}/2.35 = 1190 \text{ km s}^{-1}$).

An important caveat is that the forbidden $[\text{O III}]$ lines in the three galaxies are narrow, of order $\sigma \sim 50-70 \text{ km s}^{-1}$. In an AGN scenario this is explained by the high density of the gas close to the black hole, the forbidden lines cannot form there, because the collisional de-excitation rate exceeds the radiative de-excitation rate. Forbidden lines arise from a narrow-line region at larger distances. Interestingly, this same effect could be at work in the no-AGN scenario. We derive the density of the gas as follows. If we assume the gas and the stars follow the same spatial distribution, $r_{\text{gas}} \sim r_{\text{stars}} \sim r_e$, the ratio of the scale height to the scale length is $c/a \sim 0.5$, and $M_{\text{gas}} \sim 0.5 M_{\text{stars}}$, we obtain a gas density of $N = 10^{6.0}-10^{6.9} \text{ cm}^{-3}$, which is larger than the critical density for the forbidden line ($N_{\text{cr}, \text{O III}, 5007 \text{ \AA}} = 10^{5.8} \text{ cm}^{-3}$; I. Appenzeller & R. Oestreich 1988). If the gas disk is thinner (i.e., $c/a < 0.5$), the gas is even denser.¹⁵

5. Discussion

The main observational result of this Letter is a confirmation of the existence of extremely small ($r_e \sim 100 \text{ pc}$), luminous galaxies in the early Universe, at $z = 6-8$. Unlike other high-redshift galaxies, we know that the light at $\lambda_{\text{obs}} = 2 \mu\text{m}$ is dominated by stars, thanks to the detection of Balmer breaks in the spectra (B. Wang et al. 2024b). Despite the accurate sizes and the Balmer break detections, the densities of the galaxies remain uncertain, because AGNs might contribute to the long wavelength flux (see B. Wang et al. 2024b).

We show that the maximal mass (that is, no-AGN) models produce objects that are 1 order of magnitude denser in their

¹⁴ We note that this stellar mass is derived from photometry alone. Initial results of fitting the spectrum of this source with a stellar population show that the stellar mass is perhaps lower than this value (R. Maiolino et al. 2024a).

¹⁵ These results stem directly from the line widths: the line width is a proxy for density, and for $\sigma > 1000 \text{ km s}^{-1}$ forbidden line formation is suppressed, irrespective of the spatial scale of the gas.

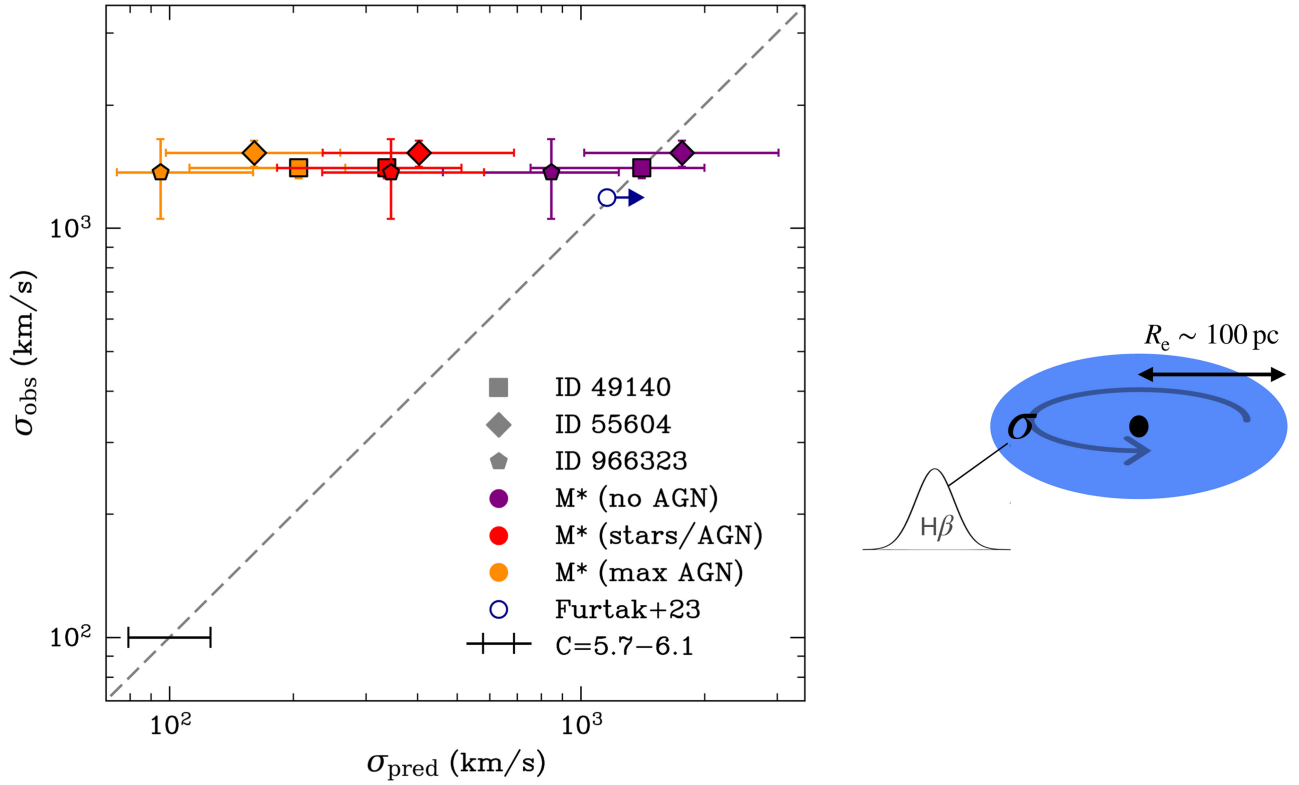


Figure 6. The observed velocity dispersion of the broad $H\beta$ lines plotted against the predicted velocity dispersion based on Equation (3) using the measured effective radius and stellar masses (Table 1). We show the three stellar mass models, $M_{*,\min}$, $M_{*,\text{med}}$, and $M_{*,\max}$ in orange, red, and purple, respectively. We predict high velocity dispersions, up to a few hundred km s^{-1} for the medium stellar mass scenario and $\sigma \gtrsim 1000 \text{ km s}^{-1}$ for the maximum stellar mass scenario, similar to the observed velocities. The black error bar in the lower left corner indicates how each measurement would shift horizontally when using different relations for Equation (3), with $C = 5.7$ (to the right) and $C = 6.1$ (to the left). In the no-AGN model, the predicted velocity dispersions are very similar to the observed $H\beta$ line widths. Perhaps, the broad Balmer emission lines in these galaxies could simply be the result of the small sizes and high masses of the galaxies. The right plot shows a schematic view of this scenario.

centers than any other known galaxies. This might be taken as evidence against such models, except that they predict line widths that correspond remarkably well to the observed broad widths of the $H\beta$ lines. If this is the correct interpretation for these galaxies, it may apply to many other “little red dots” with broad emission lines as well. It would provide a natural explanation for the lack of X-ray detections, lack of variability, and relatively faint MIRI fluxes of these galaxies (see the discussion and references in the [Introduction](#)).

It remains to be seen whether this scenario can explain all aspects of these systems. First, the high luminosity in $H\beta$ ($L > 10^{42} \text{ erg s}^{-1}$) may require an exotic mechanism for ionizing the gas. While AGNs are the most straightforward explanation, there are other possibilities. The extremely high density of the gas may lead to collisional excitation or shocks being a significant contributor (e.g., K. Davidson & T. D. Kinman 1985; B. T. Draine & C. F. McKee 1993; G. Stasińska & D. Schaerer 1999; G. Stasińska & Y. Izotov 2001; A. C. Raga et al. 2015). There is also some evidence for the presence of very massive stars at high redshift (A. Upadhyaya et al. 2024), with higher ionizing power than typical stellar populations (e.g., D. Schaerer et al. 2024a). IMFs favoring the formation of massive stars can also explain the population of bright galaxies at $z > 10$ (K. Inayoshi et al. 2022; Y. Harikane et al. 2023a; S. H. Menon et al. 2024; A. Trinca et al. 2024; L. Y. A. Yung et al. 2024). We note that alternative IMFs also change the stellar masses of the galaxies. In particular, recently P. van Dokkum & C. Conroy (2024)

proposed a “concordance IMF,” with a steep low mass slope and a shallow high mass slope. The shape of this IMF is capable of reconciling both the high-redshift bright, massive galaxies and observations of the cores of the most massive galaxies in the local Universe. This IMF produces slightly lower stellar masses ($\log(M_*) = -0.3$ to -0.2) for the three galaxies than the G. Chabrier (2003) IMF used by B. Wang et al. (2024b), but the change is much smaller than the effects of including AGNs in the modeling.

Second, the [O III] lines should be spatially extended with respect to the Balmer lines. The spatial sampling of the NIRSpect data ($0''.06$ – $0''.1$) is, however, too coarse to confidently detect this effect in the current data, but high-resolution observations (with the NIRCcam grism, or of a lensed system) should show this differential effect. Third, the line profiles of the Balmer emission lines should not be perfectly Gaussian but reflect rotation (see, e.g., P. G. van Dokkum et al. 2015). There is some evidence for asymmetries and perhaps two peaks in the medium-resolution spectra of B. Wang et al. (2024b), but this could also be interpreted as absorption (see, e.g., I. Juodžbalis et al. 2024a; B. Wang et al. 2024a). Finally, a stellar velocity dispersion measurement would be definitive. Such a case for an LRD has been reported very recently in V. Kokorev et al. (2024), a little red dot with a massive ($\log(M_*/M_\odot) \sim 10.6$) quenched galaxy host which is also compact ($r_e \leq 300 \text{ pc}$), for which a velocity dispersion of $\sigma \sim 400 \text{ km s}^{-1}$ is predicted, identical to the observed broad stellar absorption lines. There is a broad $H\beta$ absorption component, but it is too weak to

robustly determine the width of the line. A further test for these Balmer break galaxies is that for $\sigma > 1000 \text{ km s}^{-1}$ the blended absorption lines in the Balmer break region take on a smoother shape than for “normal” velocity dispersions, and this should be detectable in high signal-to-noise ratio spectra.

If this interpretation were confirmed, key questions are what might have caused such extremely small and dense galaxies to form and how they evolve into “normal” systems with larger sizes and lower central densities. Perhaps the conditions in these systems are such that feedback-free starbursts (FFBs) can occur (A. Dekel et al. 2023), with the lack of feedback leading to extreme star formation efficiencies and thereby extreme stellar masses. FFB galaxies are indeed expected to be compact (Z. Li et al. 2024). It was also recently suggested that the compactness may simply be driven by the steepness of dark matter profiles at $z = 10\text{--}14$ (M. Boylan-Kolchin 2024). Their compactness could also be the result of the low angular momentum of halos during their initial collapse, as proposed by D. J. Eisenstein & A. Loeb (1995) and A. Loeb (2024). Some general hydrodynamical simulations also produce small sizes for the most massive galaxies, such as $z \sim 6$ galaxies in TNG50 (L. Costantin et al. 2023) and $z \sim 7$ galaxies in the BLUE-TIDES simulation (M. A. Marshall et al. 2022). In addition, W. J. Roper et al. (2023) find that bulge formation begins by efficient cooling and high star formation rates in the cores down to effective radii of $r_e \sim 100 \text{ pc}$ in the FLARES simulation. However, others find discrepancies between the observed and simulated sizes of high-redshift galaxies (e.g., THESAN; X. Shen et al. 2024). It remains an open question why compactness seems to be such a generic feature of early bright star-forming galaxies ($z \sim 7\text{--}9$, $r_e \sim 100\text{--}300 \text{ pc}$; e.g., H. B. Akins et al. 2023; J. F. W. Baggen et al. 2023; W. M. Baker et al. 2024; D. Langeroodi & J. Hjorth 2023; Y. Ono et al. 2023; D. Schaerer et al. 2024b) and massive quiescent galaxies out to $z \sim 5$ ($r_e \sim 200\text{--}500 \text{ pc}$; e.g., A. C. Carnall et al. 2023; A. de Graaff et al. 2024; Z. Ji et al. 2024; V. Kokorev et al. 2024; D. J. Setton et al. 2024; L. Wright et al. 2024).

Whatever the formation mechanism, in the no-AGN scenario, dramatic evolution is required to bring the stellar mass densities in line with those of plausible descendants. One possible mechanism is adiabatic expansion due to feedback-driven mass loss from AGNs or stellar winds (L. Fan et al. 2008). Feedback may be suppressed at early times (A. Dekel et al. 2023) and then become very effective once it is “turned on.” Another mechanism is scouring by a binary SMBH (e.g., M. C. Begelman et al. 1980; J. G. Hills 1983; T. Ebisuzaki et al. 1991; G. D. Quinlan 1996) after a merger. The ejection of stars from the core lowers the density, increases the size, and likely also reduces rotational support (e.g., A. Rantala et al. 2024). While these models have been proposed to explain the size evolution of lower-redshift ($z \sim 2$) compact red nuggets, as well as the formation of cores in present-day ellipticals, they work on the right spatial scales to be relevant here. An attractive feature of such scenarios is that they act quickly, lower the central density and increase the effective radius, and keep the stellar mass roughly constant, bringing the galaxies close to observed quiescent galaxies at $z = 4\text{--}5$ (A. C. Carnall et al. 2023; A. de Graaff et al. 2024; D. J. Setton et al. 2024). After this expansion phase the galaxies slowly grow inside out, largely due to minor mergers (see, e.g., T. Naab et al. 2009;

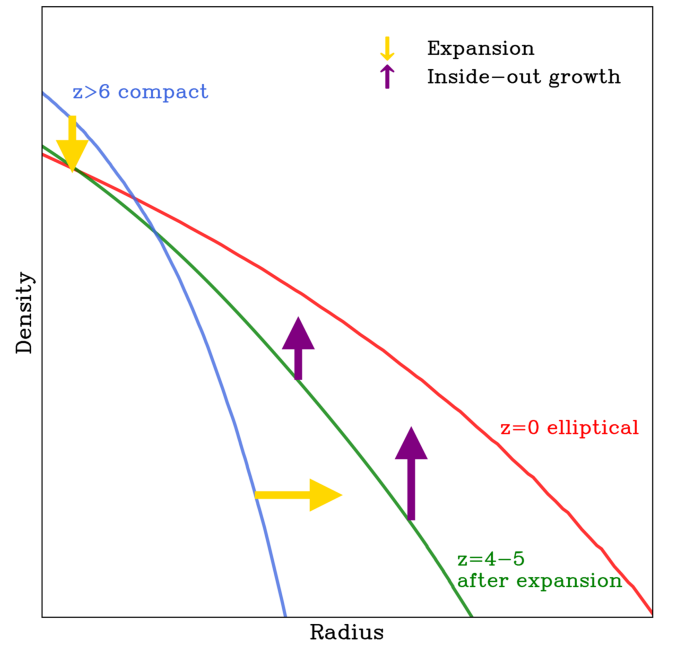


Figure 7. A possible pathway of the massive compact galaxies at $z > 6$ in the no-AGN scenario. First, a phase of expansion as a result of mass loss (triggered by feedback; e.g., L. Fan et al. 2008) or interaction of the SMBH with the stars in the central region (e.g., M. C. Begelman et al. 1980; J. G. Hills 1983; T. Ebisuzaki et al. 1991; G. D. Quinlan 1996) is required to lower the densities and velocity dispersions to those of massive compact quiescent galaxies at $z = 4\text{--}5$. After that the galaxies grow mainly in an inside-out fashion, due to minor mergers (e.g., R. Bezanson et al. 2009; T. Naab et al. 2009; P. G. van Dokkum et al. 2010).

P. G. van Dokkum et al. 2010). These pathways are illustrated in Figure 7.

It also remains to be seen whether these ultracompact galaxies are stable against gravitational collapse; it may be that parts of the galaxies collapse into SMBHs while the rest expands (D. Lynden-Bell & R. Wood 1968; see also A. Dekel et al. 2024; P. Kroupa et al. 2020).

Finally, we stress that the standard interpretation of the broad Balmer emission lines, namely, BLRs around SMBHs, remains viable—and perhaps more likely. Future observations may show whether the continuum is dominated by AGN light or stellar light, for instance, through probing the red continuum beyond $\lambda_{\text{rest}} = 1.6 \mu\text{m}$ with Atacama Large Millimeter/submillimeter Array/MIRI (see, e.g., I. Labbé et al. 2023a; H. B. Akins et al. 2024; E. Iani et al. 2024; P. G. Pérez-González et al. 2024; C. C. Williams et al. 2024). The no-AGN solution that we explore here is self-consistent and intriguing, but it requires further evidence.

Acknowledgments

We would like to thank Pablo Pérez-González, Aayush Saxena, and Avishai Dekel for useful discussions. We are also thankful for the observations made with the NASA/ESA/CSA James Webb Space Telescope and the Cosmic Evolution Early Release Science (CEERS) program (PI: Finkelstein, PID: 1345; S. L. Finkelstein et al. 2022, 2023a; see data DOI of S. L. Finkelstein et al. 2023b). The CEERS data are publicly available in the Mikulski Archive for Space Telescopes (MAST) archive at the Space Telescope Science Institute (doi:10.17909/z7p0-8481). STScI is operated by the Association of Universities for Research in Astronomy, Inc.,

under NASA contract NAS5-26555. The GRIZLI pipeline was used to reduce the data, which are available through the Dawn JWST Archive (DJA). DJA is an initiative of the Cosmic Dawn Center, which is funded by the Danish National Research Foundation under grant No. 140. Finally, we thank the anonymous referee for the useful comments on this Letter, which significantly enhanced the quality of our work.

Appendix Expected Velocity Dispersion

In this appendix, we show the derivation of Equation (3), following P. G. van Dokkum et al. (2015) and references therein.

The observed velocity dispersion of the gas, which is the second moment of the velocity distribution of the gas along the line of sight, for an unresolved rotating disk is given by

$$\sigma_{\text{gas}}^2 = \alpha^2 V_{\text{rot}}^2 \sin^2 i + \sigma_{\text{random}}^2, \quad (\text{A1})$$

where i is the inclination (such that face-on systems have $i = 0$ and edge-on disks have $i = 90$) and α is typically ~ 0.6 – 1 (M. Franx 1993; H.-W. Rix et al. 1997; B. J. Weiner et al. 2006). The random motion term contains the dispersions within the gas clouds in the interstellar medium and inclination-dependent nongravitational motions such as winds: $\sigma_{\text{random}}^2 = \sigma_{\text{ism}}^2 + w^2(i)\sigma_{\text{wind}}^2$. The rotation velocity (V_{rot}) of the gas at a radius r_{gas} is related via the virial theorem to the dynamical mass enclosed in r_{gas} :

$$V_{\text{rot, gas}}^2 = \frac{GM_{\text{dyn}}(< r_{\text{gas}})}{k r_{\text{gas}}}, \quad (\text{A2})$$

where k is the (typically radius-dependent) virial coefficient. For a perfectly spherical case, $k = 1$, but for a thin disk, a value of $k = 1.8$ (corresponding to $n = 1$) is typically used (see, e.g., L. E. Rowland et al. 2024). We assume that the stars in the compact galaxies in this work formed simultaneously with the gas, such that they have the same distribution and kinematics. Therefore, we assume that the size of the gas disk is equal to that of the stars, $r_{\text{gas}} = r_{\text{stars}} = r_e$. In principle, this might not be true at all (see the discussion in P. G. van Dokkum et al. 2015); the gas could either be more extended or more compact. If we also ignore the random motions of the gas, we obtain

$$\sigma_{\text{gas}}^2 = \alpha^2 \sin^2(i) \frac{GM_{\text{dyn}}(< r_e)}{k r_e}. \quad (\text{A3})$$








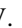


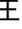


Assuming that the dynamical mass consists of gas and stars, neglecting dark matter in the center, we have $M_{\text{dyn}}(< r_e) = M_{\text{gas}}(< r_e) + M_{\text{star}}(< r_e)$. If we then assume the mass fraction in gas and stars to be equal ($f_{\text{gas}} = 0.5$), we have $M_{\text{dyn}}(< r_e) = 2M_{\text{star}}(< r_e)$, where the half-light radius contains half the stellar mass, so $M_{\text{dyn}}(< r_e) = M_{\text{star}}$. Plugging in numbers for $\alpha \sim 0.8$, $k = 1$, $i = 45^\circ$ and $G = 4.3 \times 10^{-6} \text{ kpc } (M_\odot)^{-1} (\text{km s}^{-1})^2$, we have the expected velocity dispersion of the gas, as a function of stellar mass and effective radius:

$$\log \sigma_{\text{pred}} = 0.5[\log(M_{\text{star}}) - \log(r_e) - 5.9]. \quad (\text{A4})$$

It is clear that the constant C can vary, depending on the assumed properties of the system. For example, if we assume $k = 1.8$ instead of $k = 1$, we get $C = 6.1$ (x1.25 lower velocity

dispersion), while an inclination of $i = 60^\circ$ would lead to $C = 5.7$ (x1.25 higher velocity dispersion).

ORCID iDs

Josephine F. W. Baggen  <https://orcid.org/0009-0005-2295-7246>
 Pieter van Dokkum  <https://orcid.org/0000-0002-8282-9888>
 Gabriel Brammer  <https://orcid.org/0000-0003-2680-005X>
 Anna de Graaff  <https://orcid.org/0000-0002-2380-9801>
 Marijn Franx  <https://orcid.org/0000-0002-8871-3026>
 Jenny Greene  <https://orcid.org/0000-0002-5612-3427>
 Ivo Labbé  <https://orcid.org/0000-0002-2057-5376>
 Joel Leja  <https://orcid.org/0000-0001-6755-1315>
 Michael V. Maseda  <https://orcid.org/0000-0003-0695-4414>
 Erica J. Nelson  <https://orcid.org/0000-0002-7524-374X>
 Hans-Walter Rix  <https://orcid.org/0000-0003-4996-9069>
 Bingjie Wang (王冰洁)  <https://orcid.org/0000-0001-9269-5046>
 Andrea Weibel  <https://orcid.org/0000-0001-8928-4465>

References

- Adamo, A., Bradley, L. D., Vanzella, E., et al. 2024, *Nature*, **632**, 513
 Akins, H. B., Casey, C. M., Allen, N., et al. 2023, *ApJ*, **956**, 61
 Akins, H. B., Casey, C. M., Lambrides, E., et al. 2024, arXiv:2406.10341
 Ananna, T. T., Bogdán, Á., Kovács, O. E., Natarajan, P., & Hickox, R. C. 2024, *ApJL*, **969**, L18
 Appenzeller, I., & Oestreich, R. 1988, *AJ*, **95**, 45
 Baggen, J. F. W., van Dokkum, P., Labbé, I., et al. 2023, *ApJL*, **955**, L12
 Baker, W. M., Tacchella, S., Johnson, B. D., et al. 2024, *NatAs*, Advanced Online Publication
 Balogh, M. L., Morris, S. L., Yee, H. K. C., Carlberg, R. G., & Ellingson, E. 1999, *ApJ*, **527**, 54
 Barro, G., Pérez-González, P. G., Kocevski, D. D., et al. 2024, *ApJ*, **963**, 128
 Begelman, M. C., Blandford, R. D., & Rees, M. J. 1980, *Natur*, **287**, 307
 Bezanson, R., van Dokkum, P. G., Tal, T., et al. 2009, *ApJ*, **697**, 1290
 Bogdan, Á., Goulding, A. D., Natarajan, P., et al. 2024, *NatAs*, **8**, 126
 Bouwens, R. J., Illingworth, G. D., van Dokkum, P. G., et al. 2022, *ApJ*, **927**, 81
 Boylan-Kolchin, M. 2023, *NatAs*, **7**, 731
 Boylan-Kolchin, M. 2024, arXiv:2407.10900
 Brammer, G. 2023, grizli, v1.5.2, Zenodo, doi:10.5281/ZENODO.1146904
 Bruzual, A. G. 1983, *ApJ*, **273**, 105
 Cappellari, M., Bacon, R., Bureau, M., et al. 2006, *MNRAS*, **366**, 1126
 Carnall, A. C., McLure, R. J., Dunlop, J. S., et al. 2023, *Natur*, **619**, 716
 Chabrier, G. 2003, *PASP*, **115**, 763
 Chen, Z., Stark, D. P., Endsley, R., et al. 2023, *MNRAS*, **518**, 5607
 Conroy, C., Gunn, J. E., & White, M. 2009, *ApJ*, **699**, 486
 Costantin, L., Pérez-González, P. G., Vega-Ferrero, J., et al. 2023, *ApJ*, **946**, 71
 Davidson, K., & Kinman, T. D. 1985, *ApJS*, **58**, 321
 de Graaff, A., Brammer, G., Weibel, A., et al. 2024, arXiv:2409.05948
 de Graaff, A., Setton, D. J., Brammer, G., et al. 2024, arXiv:2404.05683
 de Jong, R. S., & Lacey, C. 2000, *ApJ*, **545**, 781
 Dekel, A., Sarkar, K. C., Birnboim, Y., Mandelker, N., & Li, Z. 2023, *MNRAS*, **523**, 3201
 Dekel, A., Stone, N. C., Dutta Chowdhury, D., et al. 2024, arXiv:2409.18605
 Diamond-Stanic, A. M., Moustakas, J., Sell, P. H., et al. 2021, *ApJ*, **912**, 11
 Ding, X., Silverman, J. D., & Onoue, M. 2022, *ApJL*, **939**, L28
 Draine, B. T., & McKee, C. F. 1993, *ARA&A*, **31**, 373
 Ebisuzaki, T., Makino, J., & Okumura, S. K. 1991, *Natur*, **354**, 212
 Eisenstein, D. J., & Loeb, A. 1995, *ApJ*, **443**, 11
 Fan, L., Lapi, A., De Zotti, G., & Danese, L. 2008, *ApJL*, **689**, L101
 Finkelstein, S. L., Bagley, M. B., Arrabal Haro, P., et al. 2022, *ApJL*, **940**, L55
 Finkelstein, S. L., Bagley, M. B., Ferguson, H. C., et al. 2023a, *ApJL*, **946**, L13
 Finkelstein, S. L., Bagley, M. B., & Yang, G. 2023b, Data from The Cosmic Evolution Early Release Science Survey (CEERS) STScI/MAST, doi:10.17909/Z7P0-8481
 Franx, M. 1993, in IAU Symp. 153, Galactic Bulges, ed. H. Dejonghe & H. J. Habing (Dordrecht: Kluwer), 243
 Franx, M., van Dokkum, P. G., Förster Schreiber, N. M., et al. 2008, *ApJ*, **688**, 770

- Furtak, L. J., Labbé, I., Zitrin, A., et al. 2024, *Natur*, **628**, 57
- Furtak, L. J., Zitrin, A., Plat, A., et al. 2023, *ApJ*, **952**, 142
- Grazian, A., Castellano, M., Fontana, A., et al. 2012, *A&A*, **547**, A51
- Greene, J. E., Labbe, I., Goulding, A. D., et al. 2024, *ApJ*, **964**, 39
- Grudić, M. Y., Hopkins, P. F., Quataert, E., & Murray, N. 2019, *MNRAS*, **483**, 5548
- Hamilton, D. 1985, *ApJ*, **297**, 371
- Harikane, Y., Ouchi, M., Oguri, M., et al. 2023a, *ApJS*, **265**, 5
- Harikane, Y., Zhang, Y., Nakajima, K., et al. 2023b, *ApJ*, **959**, 39
- Heintz, K. E., Brammer, G. B., Watson, D., et al. 2024, arXiv:2404.02211
- Hills, J. G. 1983, *AJ*, **88**, 1269
- Hopkins, P. F., Murray, N., Quataert, E., & Thompson, T. A. 2010, *MNRAS*, **401**, L19
- Iani, E., Rinaldi, P., Caputi, K. I., et al. 2024, arXiv:2406.18207
- Inayoshi, K., Harikane, Y., Inoue, A. K., Li, W., & Ho, L. C. 2022, *ApJL*, **938**, L10
- Inayoshi, K., & Ichikawa, K. 2024, arXiv:2402.14706
- Ji, Z., Williams, C. C., Suess, K. A., et al. 2024, arXiv:2401.00934
- Juodžbalis, I., Ji, X., Maiolino, R., et al. 2024a, arXiv:2407.08643
- Juodžbalis, I., Maiolino, R., Baker, W. M., et al. 2024b, arXiv:2403.03872
- Kawamata, R., Ishigaki, M., Shimasaku, K., et al. 2018, *ApJ*, **855**, 4
- Killi, M., Watson, D., Brammer, G., et al. 2024, *A&A*, **691**, A52
- Kocevski, D. D., Finkelstein, S. L., Barro, G., et al. 2024, arXiv:2404.03576
- Kocevski, D. D., Onoue, M., Inayoshi, K., et al. 2023, *ApJL*, **954**, L4
- Kokorev, V., Chisholm, J., Endsley, R., et al. 2024, *ApJ*, **975**, 178
- Kokorev, V., Fujimoto, S., Labbe, I., et al. 2023, *ApJL*, **957**, L7
- Kokubo, M., & Harikane, Y. 2024, arXiv:2407.04777
- Kovács, O. E., Bogdán, Á., Natarajan, P., et al. 2024, *ApJL*, **965**, L21
- Kroupa, P., Subr, L., Jerabkova, T., & Wang, L. 2020, *MNRAS*, **498**, 5652
- Labbé, I., Greene, J. E., Bezanson, R., et al. 2023a, arXiv:2306.07320
- Labbé, I., van Dokkum, P., Nelson, E., et al. 2023b, *Natur*, **616**, 266
- Langeroodi, D., & Hjorth, J. 2023, arXiv:2307.06336
- Larson, R. L., Finkelstein, S. L., Kocevski, D. D., et al. 2023, *ApJL*, **953**, L29
- Li, Z., Dekel, A., Sarkar, K. C., et al. 2024, *A&A*, **690**, A108
- Loeb, A. 2024, *RNAAS*, **8**, 182
- Lynden-Bell, D., & Wood, R. 1968, *MNRAS*, **138**, 495
- Maiolino, R., Risaliti, G., Signorini, M., et al. 2024a, arXiv:2405.00504
- Maiolino, R., Scholtz, J., Curtis-Lake, E., et al. 2024b, *A&A*, **691**, A145
- Marshall, M. A., Wilkins, S., Di Matteo, T., et al. 2022, *MNRAS*, **511**, 5475
- Matthee, J., Naidu, R. P., Brammer, G., et al. 2024, *ApJ*, **963**, 129
- Menon, S. H., Lancaster, L., Burkhart, B., et al. 2024, *ApJL*, **967**, L28
- Naab, T., Johansson, P. H., & Ostriker, J. P. 2009, *ApJL*, **699**, L178
- Neumayer, N. 2017, in IAU Symp. 316, Formation, evolution, and survival of massive star clusters (Cambridge: Cambridge Univ. Press), **84**
- Ono, Y., Harikane, Y., Ouchi, M., et al. 2023, *ApJ*, **951**, 72
- Onoue, M., Inayoshi, K., Ding, X., et al. 2023, *ApJL*, **942**, L17
- Oschmann, J. M., Sivaramakrishnan, A., Lajoie, C.-P., et al. 2014, *Proc. SPIE*, **9143**, 91433X
- Pechetti, R., Seth, A., Neumayer, N., et al. 2020, *ApJ*, **900**, 32
- Peng, C. Y., Ho, L. C., Impey, C. D., & Rix, H.-W. 2002, *AJ*, **124**, 266
- Peng, C. Y., Ho, L. C., Impey, C. D., & Rix, H.-W. 2010, *AJ*, **139**, 2097
- Pérez-González, P. G., Barro, G., Rieke, G. H., et al. 2024, *ApJ*, **968**, 4
- Poggianti, B. M., Smail, I., Dressler, A., et al. 1999, *ApJ*, **518**, 576
- Quinlan, G. D. 1996, *NewA*, **1**, 35
- Raga, A. C., Castellanos-Ramírez, A., Esquivel, A., Rodríguez-González, A., & Velázquez, P. F. 2015, *RMxAA*, **51**, 231
- Rantala, A., Rawlings, A., Naab, T., Thomas, J., & Johansson, P. H. 2024, *MNRAS*, **535**, L202
- Rix, H.-W., Guhathakurta, P., Colless, M., & Ing, K. 1997, *MNRAS*, **285**, 779
- Roper, W. J., Lovell, C. C., Vijayan, A. P., et al. 2023, *MNRAS*, **526**, 6128
- Rowland, L. E., Hodge, J., Bouwens, R., et al. 2024, *MNRAS*, **535**, 2068
- Schaerer, D., Guibert, J., Marques-Chaves, R., & Martins, F. 2024a, arXiv:2407.12122
- Schaerer, D., Marques-Chaves, R., Xiao, M., & Korber, D. 2024b, *A&A*, **687**, L11
- Schödel, R., Merritt, D., & Eckart, A. 2009, *A&A*, **502**, 91
- Sersic, J. L. 1968, Atlas de Galaxias Australes (Cordoba: Observatorio Astronomico)
- Setton, D. J., Khullar, G., Miller, T. B., et al. 2024, *ApJ*, **974**, 145
- Shen, X., Vogelsberger, M., Borrow, J., et al. 2024, *MNRAS*, **534**, 1433
- Shibuya, T., Ouchi, M., & Harikane, Y. 2015, *ApJS*, **219**, 15
- Silk, J., Begelman, M. C., Norman, C., Nusser, A., & Wyse, R. F. G. 2024, *ApJL*, **961**, L39
- Stasińska, G., & Izotov, Y. 2001, *A&A*, **378**, 817
- Stasińska, G., & Schaerer, D. 1999, *A&A*, **351**, 72
- Tal, T., van Dokkum, P. G., Nelan, J., & Bezanson, R. 2009, *AJ*, **138**, 1417
- Taylor, E. N., Franx, M., Brinchmann, J., van der Wel, A., & van Dokkum, P. G. 2010, *ApJ*, **722**, 1
- Topping, M. W., Stark, D. P., Senchyna, P., et al. 2024, *MNRAS*, **529**, 3301
- Trinca, A., Schneider, R., Valiante, R., et al. 2024, *MNRAS*, **529**, 3563
- Übler, H., Maiolino, R., Curtis-Lake, E., et al. 2023, *A&A*, **677**, A145
- Upadhyaya, A., Marques-Chaves, R., Schaerer, D., et al. 2024, *A&A*, **686**, A185
- van der Wel, A., Franx, M., Wuyts, S., et al. 2006, *ApJ*, **652**, 97
- van Dokkum, P., & Conroy, C. 2024, *ApJ*, **973**, L32
- van Dokkum, P. G., Nelson, E. J., Franx, M., et al. 2015, *ApJ*, **813**, 23
- van Dokkum, P. G., Whitaker, K. E., Brammer, G., et al. 2010, *ApJ*, **709**, 1018
- Wang, B., de Graaff, A., Davies, R. L., et al. 2024a, arXiv:2403.02304
- Wang, B., Leja, J., de Graaff, A., et al. 2024b, *ApJL*, **969**, L13
- Wang, T., Sun, H., Zhou, L., et al. 2024c, arXiv:2403.02399
- Weaver, J. R., Cutler, S. E., Pan, R., et al. 2024, *ApJS*, **270**, 7
- Weibel, A., Oesch, P. A., Barrufet, L., et al. 2024, *MNRAS*, **533**, 1808
- Weiner, B. J., Willmer, C. N. A., Faber, S. M., et al. 2006, *ApJ*, **653**, 1027
- Williams, C. C., Alberts, S., Ji, Z., et al. 2024, *ApJ*, **968**, 34
- Williams, H., Kelly, P. L., Chen, W., et al. 2023, *Sci*, **380**, 416
- Worthey, G., Faber, S. M., Gonzalez, J. J., & Burstein, D. 1994, *ApJS*, **94**, 687
- Wright, L., Whitaker, K. E., Weaver, J. R., et al. 2024, *ApJL*, **964**, L10
- Yang, L., Morishita, T., Leethochawalit, N., et al. 2022, *ApJL*, **938**, L17
- Yue, M., Eilers, A.-C., Ananna, T. T., et al. 2024, *ApJL*, **974**, L26
- Yung, L. Y. A., Somerville, R. S., Finkelstein, S. L., Wilkins, S. M., & Gardner, J. P. 2024, *MNRAS*, **527**, 5929
- Zhang, H.-X., Peng, E. W., Côté, P., et al. 2015, *ApJ*, **802**, 30